

On the Fracture and Fatigue Properties of Mo-Mo₃Si-Mo₅SiB₂ Refractory Intermetallic Alloys at Ambient to Elevated Temperatures (25 °C to 1300 °C)

H. CHOE, J.H. SCHNEIBEL, and R.O. RITCHIE

The need for structural materials with high-temperature strength and oxidation resistance coupled with adequate lower-temperature toughness for potential use at temperatures above ~1000 °C has remained a persistent challenge in materials science. In this work, one promising class of intermetallic alloys is examined, namely, boron-containing molybdenum silicides, with compositions in the range Mo (bal), 12 to 17 at. pct Si, 8.5 at. pct B, processed using both ingot (I/M) and powder (P/M) metallurgy methods. Specifically, the oxidation (“pestring”), fracture toughness, and fatigue-crack propagation resistance of four such alloys, which consisted of ~21 to 38 vol. pct α -Mo phase in an intermetallic matrix of Mo₃Si and Mo₅SiB₂ (T₂), were characterized at temperatures between 25 °C and 1300 °C. The boron additions were found to confer improved “pest” resistance (at 400 °C to 900 °C) as compared to unmodified molybdenum silicides, such as Mo₅Si₃. Moreover, although the fracture and fatigue properties of the finer-scale P/M alloys were only marginally better than those of MoSi₂, for the I/M processed microstructures with coarse distributions of the α -Mo phase, fracture toughness properties were far superior, rising from values above 7 MPa \sqrt{m} at ambient temperatures to almost 12 MPa \sqrt{m} at 1300 °C. Similarly, the fatigue-crack propagation resistance was significantly better than that of MoSi₂, with fatigue threshold values roughly 70 pct of the toughness, *i.e.*, rising from over 5 MPa \sqrt{m} at 25 °C to ~8 MPa \sqrt{m} at 1300 °C. These results, in particular, that the toughness and cyclic crack-growth resistance actually increased with increasing temperature, are discussed in terms of the salient mechanisms of toughening in Mo-Si-B alloys and the specific role of microstructure.

I. INTRODUCTION

IN the search for higher temperature structural materials to replace nickel-based superalloys for future propulsion systems, transition-metal silicides have received considerable recent interest.^[1–7] These alloys constitute a unique class of ultrahigh-temperature intermetallic materials, with high melting points (molybdenum and titanium silicides have melting points in excess of 2000 °C) and the capability of forming protective silicon oxide films for enhanced oxidation resistance at elevated temperatures in hostile environments. In addition, specific silicides, such as Mo₅Si₃ (T₁), have excellent creep resistance at temperatures as high as 1400 °C.^[2] Despite these advantages, most refractory silicides invariably display very poor fracture toughness at low temperatures^[3,4] and can be susceptible to oxidation problems (“pest” reactions*) at temperatures below ~1000 °C.^[8,9,10]

*The pest reaction, *i.e.*, accelerated oxidation at intermediate temperatures, is generic to all forms of molybdenum silicides. For example, MoSi₂ is prone to pest reaction in air between 300 °C and 600 °C,^[8,9] whereas monolithic Mo₅Si₃ exhibits severe pest reaction at 800 °C.^[12,14]

H. CHOE, formerly Graduate Student with the Materials Sciences Division, Lawrence Berkeley National Laboratory, and Department of Materials Science and Engineering, University of California, Berkeley, is Postdoctoral Researcher, Northwestern University, Evanston, IL 60208. J.H. SCHNEIBEL, Senior Scientist, is with the Metals and Ceramics Division, Oak Ridge National Laboratory, Oak Ridge, TN 37831-6115. R.O. RITCHIE, Professor, is with the Materials Sciences Division, Lawrence Berkeley National Laboratory, and Department of Materials Science and Engineering, University of California, Berkeley, CA 94720. Contact e-mail: RORitchie@LBL.gov

Manuscript submitted April 23, 2002.

A potential solution to these problems may be provided by the boron-modified molybdenum silicide system.^[11] These alloys generally consist of thermodynamically stable two-phase mixtures of Mo and Mo₅SiB₂ (T₂) or three-phase mixtures of Mo, Mo₅SiB₂, and Mo₃Si, have high melting temperatures above ~2000 °C, improved low-temperature fracture toughness properties (compared to MoSi₂),^[3,7] and excellent high-temperature oxidation resistance that increases with increasing boron content.^[12–18] Indeed, in contrast to MoSi₂ and Mo₅Si₃, which are very prone to pest reactions,^[10,12,14] tertiary Mo-Si-B alloys have a reduced susceptibility to such intermediate temperature oxidation due to the formation of a protective borosilicate layer.^[12–14,16–18] However, as the compositions that promote such oxidation resistance, *i.e.*, higher B and Si, may not be the ones that promote toughness, *i.e.*, higher Mo, optimization of these alloys requires a trade-off between crack growth and oxidation resistance. Although several recent studies have focused on the oxidation and pestring properties of Mo-Si-B alloys,^[8–10,11–18] little research has been devoted to their fracture and fatigue properties, particularly at elevated temperatures above 1000 °C.

In an earlier study,^[7] we examined the fracture toughness and fatigue-crack propagation behavior of one such alloy, Mo-12Si-8.5B (at. pct), at ambient and elevated temperatures. In the current work, we compare the results from this alloy with those from a series of other boron-doped molybdenum silicide alloys with varying chemistries and microstructures at temperatures between 25 °C and 1300 °C. These alloys, which all consisted of α -Mo and the intermetallic phases Mo₃Si and Mo₅SiB₂, are based on a similar composition, but some with higher Si and lower Mo concen-

trations for oxidation resistance, and another with Nb additions^[3] for solid-solution strengthening of the α -Mo to improve creep strength. Since the coarseness of microstructure can have a marked influence on the fracture and fatigue properties, both ingot (I/M) and powder metallurgy (P/M) processing were employed to significantly vary the characteristic microstructural dimensions.

Due to the extreme brittleness of refractory silicides, principal emphasis is given to the understanding of the effect of microstructure on toughening behavior, as this is clearly a limiting feature in the design of Mo-Si-B alloys with acceptable properties. Particular attention is given to the morphology and composition of the individual phases, especially the α -Mo phase, as this has been recently shown to play a central role in determining fracture properties of alloys containing the α -Mo, Mo₃Si, and Mo₅SiB₂ phases.^[7] In the present work, it is similarly found that, mechanistically, crack trapping and ductile-phase bridging by the α -Mo phase and microcracking within the Mo₅SiB₂ phase provide the major contributions to crack-growth resistance, with the coarser-grained I/M Mo-12Si-8.5B alloy having the best crack-growth properties with a reduced susceptibility to lower-temperature pest reactions as compared to molybdenum silicides without boron.

II. EXPERIMENTAL PROCEDURES

A. Processing and Microstructure

Four alloys, of composition (in at. pct) Mo-12Si-8.5B (termed alloy IM1), Mo-16.8Si-8.4B (alloys PM1 and PM2), and Mo-12Si-10Nb-8.5B (alloy IM2), were prepared from elemental Mo, Si, B, and Nb, which were, respectively, 99.95, 99.99, 99.5, and 99.8 wt. pct pure. Alloys IM1 and IM2 were directly prepared by arc melting ~500 g of the starting materials into a water-cooled 25-mm-diameter copper mold; the castings were then homogenized by annealing *in vacuo* for 24 hours at 1600 °C. As noted previously, Nb was added as a solid solution strengthener to alloy IM2 to harden the α -Mo phase.

Alloys PM1 and PM2, conversely, were processed using powder-metallurgy methods. The rationale for this was twofold: (1) to improve oxidation resistance by reducing the α -Mo volume fraction through increases in the Si content, which can cause severe cracking during melting and casting in I/M processing, and (2) to discern how much the fracture toughness is compromised by such reductions in the Mo content. Alloy PM1 was prepared by first arc casting several 500 g buttons with the composition Mo-16.8Si-8.4B; the resulting ingots were then crushed into -60/+230 mesh (63 to 250 μ m) powder. The powder was filled into a Nb hot-isostatic pressing ("HIPing") can, which was sealed by electron beam welding, consolidated in argon at 1600 °C and 200 MPa for 2 hours, and subsequently annealed *in vacuo* for 24 hours at 1600 °C. Alloy PM2 was prepared by arc casting several 500 g buttons with the composition Mo-20Si-10B, which were crushed into -100/+270 mesh (53 to 150 μ m) powder. The powder was then mixed with an appropriate quantity of 2 to 8 μ m Mo powder to give a nominal composition Mo-16.8-8.4B. Because of a leak in the Nb can, initial HIPing of the powder mixture was not successful; however, hot pressing for 2 hours in a graphite die *in vacuo* at 1800 °C at 35 MPa pressure resulted in

almost complete consolidation. The hot-pressed material was subsequently containerless HIPed and annealed in the same way as alloy PM1 (Table I). Further details on the processing and microstructure characterization of these materials are reported elsewhere;^[5,6,7] a general summary of the powder processing of silicides can be found in Reference 19.

B. Cyclic Fatigue Testing

Cyclic fatigue-crack growth behavior in the Mo-12Si-8.5B alloys was examined both at ambient temperature in a controlled room-air environment and elevated temperatures (25 °C to 1300 °C) in flowing gaseous argon. Testing was conducted under tension-tension loading using ~2.8-mm-thick, disk-shaped compact-tension DC(T) specimens (of width ~18 mm), containing "large" (>3 mm) through-thickness cracks. Specimens were cycled under stress-intensity control on computer-controlled servohydraulic testing machines at a load ratio (ratio of minimum to maximum loads) of $R = 0.1$ with a test frequency of 25 Hz (sine wave). Procedures essentially conform to ASTM Standard E647,^[20] although modified for the testing of brittle materials.^[21] Crack-growth rates, da/dN , were obtained over the range $\sim 10^{-11}$ to 10^{-5} m/cycle under both K -decreasing and K -increasing conditions, with a normalized K gradient of ± 0.1 mm⁻¹.^[20] Data are presented in terms of the growth rate per cycle as a function of applied stress-intensity range, given by the difference in the maximum and minimum stress intensities during the cycle ($\Delta K = K_{\max} - K_{\min}$). Fatigue thresholds, ΔK_{th} and $K_{\max, \text{th}}$, below which large cracks are presumed to grow at vanishingly small rates, were defined as the maximum value of the appropriate stress intensity at which growth rates did not exceed 10^{-11} m/cycle.

Prior to data collection, samples were fatigue precracked at room temperature for at least 1 mm beyond the notch. Precracking was facilitated using a half-chevron shaped notch that was sharpened using a razor micronotching technique. Further details are given in Reference 7.

For room-temperature testing, crack lengths were continuously monitored *in situ* using unloading elastic compliance based on the back-face strain; measurements were made with a 350- Ω back-face strain gauge and utilized the calibrations for the DC(T) sample given in Reference 22. At elevated temperatures between 800 °C and 1300 °C, electrical potential-drop methods were alternatively used to monitor crack lengths.^[23,24] Specifically, a constant direct current of ~2 A was applied to the sample, such that an initial amplified output potential of ~0.4 to 0.6 V was developed across the starter crack. With crack extension, subsequent changes in output potential were normalized by the initial potential, and then continuously monitored to permit *in situ* monitoring of the crack length using the potential calibrations derived in Reference 22. Full details of this application of electrical-potential techniques to crack length monitoring at temperatures up to 1300 °C are presented elsewhere.^[23]

C. Resistance-Curve Measurements

Fracture toughness behavior was evaluated under plane-strain conditions by monotonically loading fatigue-precracked, disk-shaped compact-tension DC(T) specimens to failure. During such tests, crack lengths were periodically

Table I. Composition of Mo-Si-B Alloys Examined

Alloy	Composition (At. Pct)	Processing
IM 1	Mo-12Si-8.5B	ingot metallurgy, arc melting, and casting
IM 2	Mo-12Si-10Nb-8.5B	ingot metallurgy, arc melting, and casting
PM 1	Mo-16.8Si-8.4B	powder metallurgy with Mo-16.8Si-8.4B
PM 2	Mo-16.8Si-8.4B	powder metallurgy with Mo-20Si-10B and Mo

monitored using the same elastic unloading compliance (at 25 °C) and electrical-potential (at 800 °C to 1300 °C) methods described previously, although unloading excursions were limited to less than 10 pct of the current load. Following precracking, specimens were cycled for ~24 hours at the ΔK_{th} threshold (where there is no discernable crack growth) in an attempt to remove any possible crack bridging in the wake of the precrack. The resistance curve (*R*-curve) behavior was then evaluated by measuring the crack-growth resistance, K_R , as a function of crack extension, Δa .

D. Metallography and Fractography

The microstructures of the Mo-Si-B alloys were evaluated using optical and scanning electron microscopy, following mechanical polishing and etching in Murakami's reagent (aqueous solution of potassium ferricyanide and sodium hydroxide). This etchant selectively attacks Mo_5SiB_2 (T_2) and hence can be used to differentiate between the T_2 and Mo_3Si phases, which have nearly the same back-scattered electron contrast. These phases were identified both by energy-dispersive spectroscopy (EDS, Noran 5502, Middleton, WI) and powder X-ray diffraction (XRD, Siemens Diffraktometer, New York, NY). The contiguous nature of the α -Mo phase was assessed metallographically using the analysis described in the Appendix. The contiguity parameters ($N_L^{\alpha\alpha}$ and $N_L^{\alpha\beta}$)* needed to calculate the contiguity C_α of

*For the definition of these parameters for the Mo-Si-B alloys, the α -Mo phase is denoted as the " α phase," while the matrix of intermetallic Mo_3Si and Mo_5SiB_2 phases is denoted as the " β phase."

the α -Mo in each microstructure were experimentally measured using standard metallographic methods. Ten random lines of unit length were drawn on the examined plane of polish for each microstructure and simple intercept measurements were conducted to obtain average values of both $N_L^{\alpha\alpha}$ and $N_L^{\alpha\beta}$.

Fatigue and fracture surfaces were imaged in a scanning electron microscope (SEM). In addition, crack-path profiles were obtained by examining polished and etched metallographic sections cut perpendicular to the fracture surfaces.

E. Oxidation/Pesting Behavior of Mo-Si-B Alloy

To assess the oxidation resistance of the Mo-Si-B alloy at the intermediate temperatures (400 °C to 900 °C) where pest reactions can occur, static oxidation tests were carried out on the alloy IM1. Small coupons measuring $\sim 10 \times 10 \times 1$ mm were sectioned from HIPed samples, polished in successive steps to a 1- μm finish, ultrasonically cleaned in water, and then rinsed successively in ethanol and acetone prior to drying in air. The initial size and weight of each coupon were carefully measured and they were then placed in high-purity alumina boats in such a way as to minimize

contact. The coupons were exposed for a fixed length of time at a constant temperature in an air furnace, having been inserted into the furnace chamber 2 hours after the desired temperature had been reached. They were then periodically weighed to observe the transient weight change and to determine isothermal oxidation rates. The static oxidation resistance was estimated by dividing the weight change of the coupons after exposure by their surface area. Oxidation scales and phases after exposure were evaluated using XRD and EDS.

III. RESULTS

A. Microstructure

Microstructures and particle size distributions of α -Mo phase in the four boron-modified molybdenum silicide alloys developed for the present study are shown, respectively, in Figure 1 and Table II. All alloy microstructures have three phases: α -Mo (bcc structure), Mo_3Si (cubic A15) and Mo_5SiB_2 (T_2) (tetragonal D8₁). The I/M alloys consist of ~38 vol. pct of α -Mo with roughly 30 vol pct of each of the two intermetallic phases; the P/M alloys, conversely, contain a significantly lower α -Mo volume fraction (~21 pct). Specifically, the differences in the four alloys lie in the volume fraction, size, and distribution (specifically the contiguity) of the α -Mo phase, which is most prevalent in the I/M alloys (Table II).

- (1) IM1 alloy: This Mo-12Si-8.5B alloy has the coarsest microstructure, with the largest average α -Mo particle size of $\sim 10 \mu m$ (range from ~ 0.5 to $100 \mu m$) within a brittle intermetallic Mo_3Si/Mo_5SiB_2 matrix. The α -Mo generally exists as a discrete and discontinuous phase, as in all four alloys; however, in the IM1 alloy, there is the highest number of large ($>30 \mu m$) α -Mo particles, which often form semicontinuous Mo phase regions (Figure 1(a)). Indeed, the contiguity of the α -Mo phase is highest in this alloy ($C_\alpha = 0.31$), being almost 3 times that in the PM1 alloy (Table II).
- (2) IM2 alloy: Despite the difference in composition due to the addition of 10 at. pct Nb,* the microstructure of this

*Essentially, Nb dissolves in all three phases (α -Mo, Mo_3Si , and Mo_5SiB_2), which leads to an increase in their lattice parameters as Nb has a larger atomic radius than Mo for which it substitutes.^[3]

Mo-12Si-10Nb-8.5B alloy (Figure 1(d)) is quite similar to that of IM1. However, the contiguity of the Mo phase is somewhat lower ($C_\alpha = 0.25$), and the average size of α -Mo phase is somewhat smaller ($\sim 7 \mu m$). Indeed, the less continuous distribution of α -Mo phase and its smaller average size is reasoned to be a prime reason for its lower fracture toughness compared to that of alloy IM1. An additional factor is the hardening of the α -Mo phase by Nb. Whereas the Vickers hardness of alloy

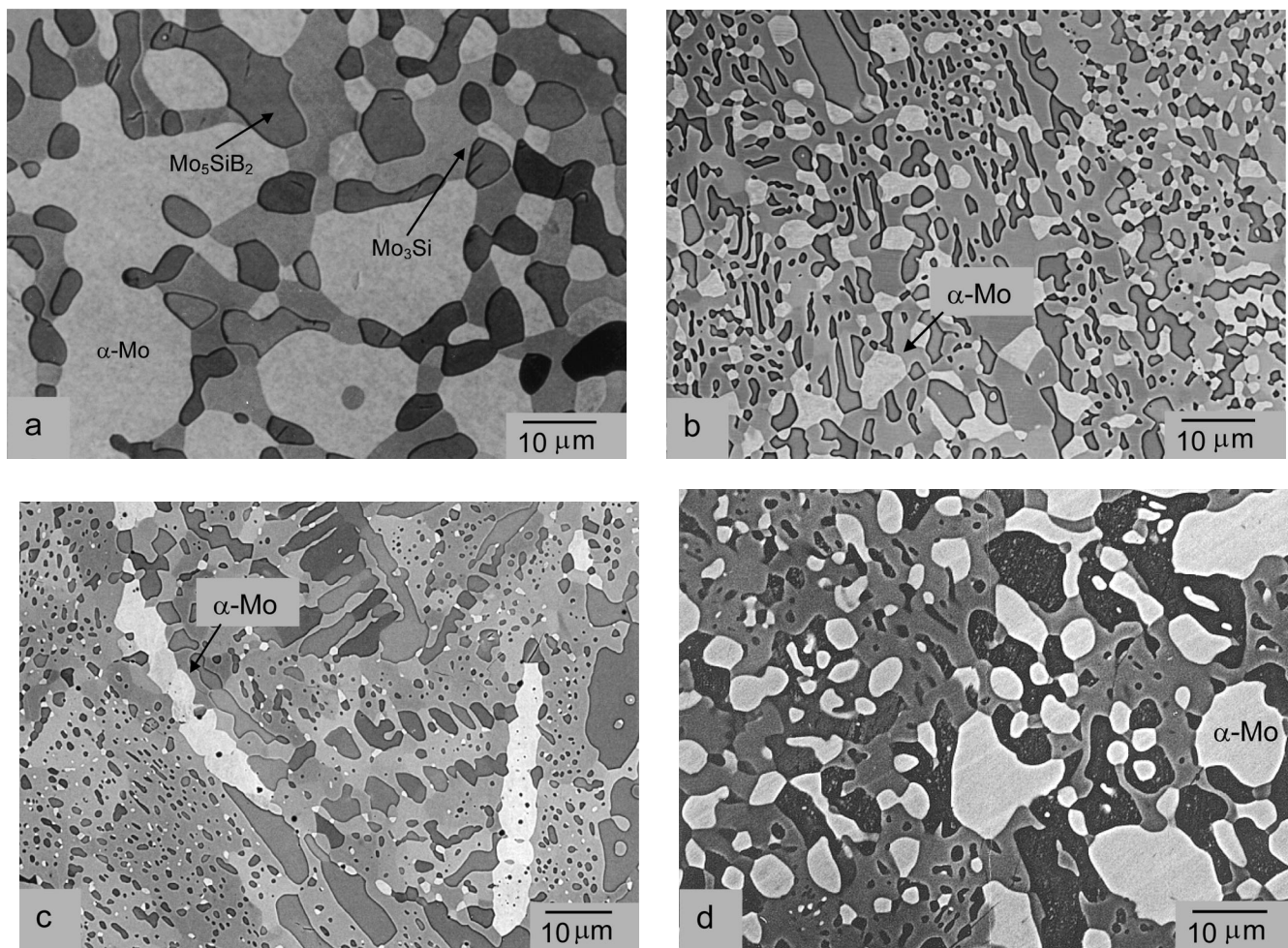


Fig. 1—Scanning electron micrographs of the microstructures in the Mo-Si-B alloys examined, showing (a) cast IM1 alloy; (b) PM1 alloy, processed by HIPing crushed Mo-16.8Si-8.4B powders; (c) PM2 alloy, processed by HIPing the mixture of crushed Mo-20Si-10B particles and Mo powders; and (d) cast IM2 alloy (etchant: Murakami's reagent).

Table II. α -Mo Particle Size Distributions

Alloy	Volume Fraction of α -Mo Phase (Pct)	Average Size of α -Mo Phase (μm)	Standard Deviation (μm)	Maximum Size (μm)	Minimum Size (μm)	Contiguity C_α of α -Mo*
IM1	38	10.43	16.37	100	0.5	0.31
IM2	38	6.99	10.83	50	0.5	0.25
PM1	21	2.14	2.03	8	0.5	0.13
PM2	21	4.41	11.21	60**	0.5	0.20

*Contiguity C_α of the α -Mo phase is defined in the Appendix

**As the largest α -Mo particles in the PM2 microstructure have an elongated shape with aspect ratios between ~ 5 to 10, the diameter of the maximum particle is defined as an average of the largest and the smallest diameters.

IM1 (for 10-g indents in the larger α -Mo particles) was 212 ± 10 , that of alloy IM2 was 258 ± 16 . Consequently, it is believed that hardening by the Nb likely reduces the fracture toughness of the α -Mo, and thereby the fracture toughness of alloy IM2.

(3) PM1 and PM2 alloys: Both these alloys have nominally identical compositions (Mo-16.8Si-8.4B) despite being processed by different routes; their respective microstructures are shown in Figures 1(b) and (c). They have much higher oxygen concentrations than the corresponding I/M alloys (Table III), especially alloy PM2, which

Table III. Carbon, Nitrogen, and Oxygen Contents (wppm) Determined from LECO* Inert Gas Fusion

Alloy	C	N	O
IM1	127	80	172
IM2	90	20	40
PM1	10	10	590
PM2	90	40	1980

*LECO is a trademark of LECO Corporation, St. Joseph, MI.

was consolidated in several steps and consequently had a particularly high oxygen content. These alloys also have significantly finer microstructures than the corresponding I/M alloys, with a lower α -Mo content. Alloy PM1 consists of a uniform distribution of fine α -Mo particles (average size $\sim 2 \mu\text{m}$) within a brittle $\text{Mo}_3\text{Si}/\text{Mo}_5\text{SiB}_2$ matrix, with little contiguity of particles ($C_\alpha = 0.13$). Alloy PM2, obtained by HIPing crushed Mo-20Si-10B particles with fine Mo powders, displays an extreme distribution of the Mo phase, consisting of either small ($\sim 1 \mu\text{m}$) or large ($\sim 50 \mu\text{m}$) particles with an average size of $\sim 4.41 \mu\text{m}$. The finer α -Mo particles are relatively equiaxed in shape, whereas the larger particles tend to be elongated (aspect ratio ~ 5 to 10). The contiguity of the α -Mo phase ($C_\alpha = 0.20$) was smaller than in the I/M alloys but ~ 50 pct higher than in the PM1 alloy.

B. Pest Reaction

Molybdenum silicide alloys are known to be susceptible to oxidation (or “pestering”^[2,8,12,14,15]) at intermediate temperatures ($\sim 300^\circ\text{C}$ to 800°C), which results from a competition between the formation and volatilization of MoO_3 , which begins at lower temperatures, with the formation of a continuous protective passivating SiO_2 layer at higher temperatures. The pest problem generally arises at the lower temperatures, as the protective oxide layers that form there have insufficient fluidity to effectively cover microcracks created by the large dilation associated with the oxide formation. This problem is generic to all forms of molybdenum silicides^[14–18] and, under constant temperature (static oxidation) conditions, is typically characterized by a brief initial period of fairly rapid weight gain, an intermediate period of several hours of duration where the weight changes little with time, and finally a period of accelerating rate of weight loss.

Since MoSi_2 is highly susceptible to pesting at $\sim 300^\circ\text{C}$ to 600°C (the bulk material can be completely reduced to powder after less than 100 hours exposure in air^[8,9,12]), the static oxidation properties of the current IM1 alloy were examined between 400°C and 900°C . Results are shown in Figure 2 for 50-hour exposures in air and are compared to those for monolithic Mo_5Si_3 at 800°C .^[12] It is apparent that compared to Mo_5Si_3 , the kinetics of the pest reaction in the Mo-Si-B alloy was significantly slowed at these temperatures.

Specifically, oxidation rates were negligible at 400°C to 600°C because samples showed no change in weight or appearance. The formation of the MoO_3 scale in this alloy is negligible below 600°C ; indeed, XRD studies did not reveal any molybdenum or silicon oxide scales either at 400°C or 500°C , except for a thin white surface layer of MoO_3 at 600°C . At 700°C , MoO_3 was also detected, and the small, but finite, measured weight loss, coupled with some degree of shape change (inset, Figure 2), at this temperature can be attributed to the onset of MoO_3 evaporation. At 800°C , the largest weight loss was seen with some degree of distortion and delamination of the specimen (inset, Figure 2), due to the sublimation of the MoO_3 , which becomes significant above $\sim 750^\circ\text{C}$.^[14,16] These results are consistent with recent pesting studies on these alloys by Mendiratta and co-workers.^[16,25] However, the weight change was not

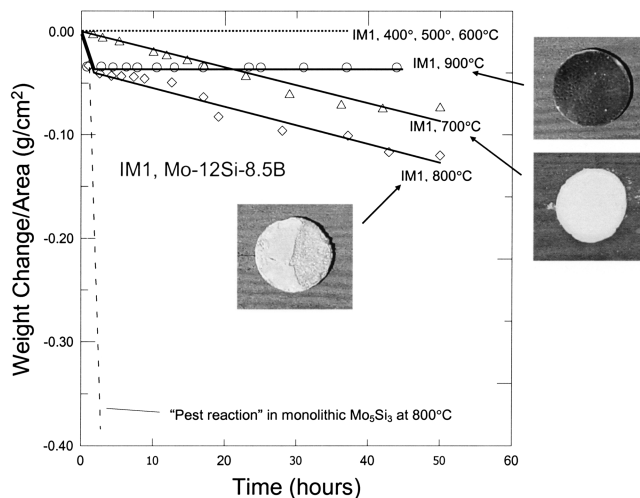


Fig. 2—Static oxidation behavior of IM1 alloy (Mo-12Si-8.5B) in air at 700°C , 800°C , and 900°C , as compared to “pestering” in monolithic Mo_5Si_3 at 800°C ,^[12] showing weight change as a function of time at temperatures. Insets show the surface appearance of the scale on test samples after ~ 50 h exposure at the temperature indicated.

large as compared to Mo_5Si_3 , due to the formation of a nearly continuous layer of borosilicate glass ($\text{B}_2\text{O}_3/\text{SiO}_2$) at $\sim 800^\circ\text{C}$, which provides a degree of protection that increases with increasing temperature. As this B-containing silica glass exhibits a lower viscosity than silica itself, with a higher diffusion rate for oxygen, it can form more rapidly and flow into cracks and voids on the alloy surface to provide greater oxidation protection.^[13,26] This is particularly apparent at 900°C where the large surface pores caused by severe volatilization of MoO_3 were covered by a liquidlike borosilicate glass layer (inset, Figure 2). This resulted in an improved oxidation protection with the weight change at 900°C lower than either at 700°C or 800°C . X-ray diffraction analysis also revealed the presence of the MoO_2 phase on the surfaces at 900°C .

These results suggest that Mo-Si-B alloys possess a better pesting resistance as compared to non-B-containing molybdenum silicides, due to minimal MoO_3 formation below $\sim 700^\circ\text{C}$ and protection by the $\text{B}_2\text{O}_3/\text{SiO}_2$ scale above $\sim 800^\circ\text{C}$. However, the oxidation resistance of these alloys at and just below 800°C is still of some concern with weight losses that are not insignificant. Moreover, the pesting resistance can be quite sensitive to small variations in temperature, and factors such as the local composition, the degree of pre-existing pores or cracks, *etc.* can cause changes in the oxidation behavior. In addition, at very high temperatures above $\sim 1500^\circ\text{C}$, the viscosity of the borosilicate glass can decrease so much that dripping of the scale takes place; this naturally leads to the protection capability of the glass to be considerably diminished.^[13] Clearly, the oxidation resistance of these alloys is far from optimized and does require further study.

C. Fracture Toughness Behavior

The fracture toughness properties of the four Mo-Si-B alloys were determined at temperatures between ambient and 1300°C in terms of their resistance-curve behavior.

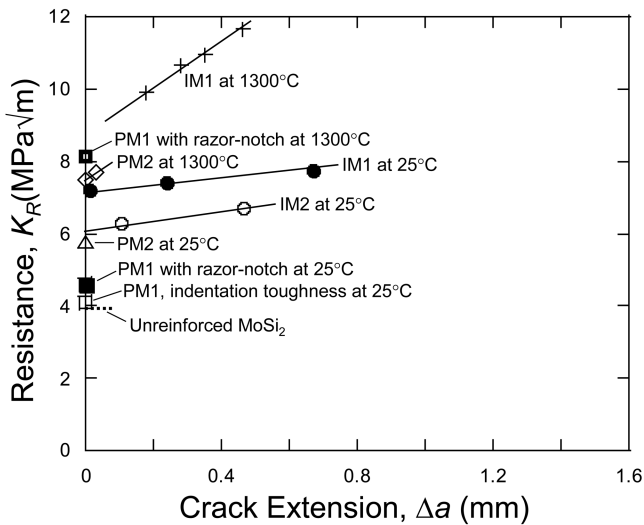


Fig. 3—Fracture toughness and R -curve behavior of Mo-Si-B alloys, showing crack-growth resistance, K_R , plotted as a function of crack extension, Δa , for the I/M and P/M alloys at 25 °C and 1300 °C. Results for the borron-modified molybdenum silicides are compared with previous data^[4] on monolithic MoSi_2 .

From the results, which are plotted in Figure 3, several points are worthy of note.

- (1) Both I/M alloys displayed some degree of rising R -curve behavior at all temperatures with subcritical crack growth extending for ~ 200 to $800 \mu\text{m}$; this effect is relatively minor, however, at 25 °C. Such R -curve behavior is not shown by either of the P/M alloys, which failed catastrophically with little or no subcritical crack growth once the stress intensity exceeded the crack-initiation toughness, $K_0 = K_{Ic}$. The latter behavior is characteristic of monolithic MoSi_2 and Nb-particulate reinforced MoSi_2 .^[4]
- (2) With the exception of the PM1 alloy, all Mo-Si-B alloys displayed at least a 50 pct higher fracture toughness than MoSi_2 ^[4] at ambient temperatures. The I/M alloys were significantly tougher than the P/M alloys, consistent with their higher α -Mo volume fraction, larger α -Mo particle size, and higher contiguity of the α -Mo phase.
- (3) The highest toughness was shown by the IM1 alloy, which had a crack-initiation toughness at 25 °C of $K_0 \sim 7.2 \text{ MPa}\sqrt{\text{m}}$, rising over $\sim 800 \mu\text{m}$ of crack extension to a steady-state (plateau) toughness of $K_{ss} \sim 7.8 \text{ MPa}\sqrt{\text{m}}$, *i.e.*, some ~ 80 to 95 pct higher than that for monolithic MoSi_2 (where $K_{Ic} \sim 4 \text{ MPa}\sqrt{\text{m}}$). In comparison, the finer-grained IM2 alloy had ~ 13 pct lower toughness than IM1 at 25 °C, with crack initiation and steady-state values of 6.3 and 6.7 $\text{MPa}\sqrt{\text{m}}$, respectively.
- (4) Both P/M alloys were considerably more brittle than the I/M alloys. The PM2 alloy fractured catastrophically at crack initiation at $K_{Ic} = 5.7 \text{ MPa}\sqrt{\text{m}}$. The PM1 alloy was so brittle that it could not even be fatigue precracked (at 25 °C or 1300 °C). Based on crack initiation from a sharpened razor notch, an overestimate of K_{Ic} was measured at 4.3 $\text{MPa}\sqrt{\text{m}}$, consistent with an approximate indentation toughness measurement of 4.1 $\text{MPa}\sqrt{\text{m}}$; these values are essentially the same as that of unreinforced molybdenum disilicide. The P/M alloys show clearly the important effect of the microstructural

scale and topology. They both contain the same volume fraction of the α -Mo phase, but alloy PM2 has a significantly higher fracture toughness as most of the α -Mo occurs in the form of large ($\sim 50 \mu\text{m}$) elongated particles. These large particles provide effective toughening even though the high oxygen content of alloy PM2 would suggest embrittlement of the α -Mo in this alloy. It should also be pointed out that alloy PM1 was engineered for high oxidation resistance (*i.e.*, it contains only fine α -Mo particles). A coupon annealed in air for 1 day at 1300 °C exhibited a weight loss of 6 mg/cm^2 , whereas the corresponding value for alloy PM2 was 220 mg/cm^2 .^[27]

- (5) With increasing temperature, the fracture toughness of all four Mo-Si-B alloys increased. At 1300 °C, the two P/M alloys displayed K_{Ic} values of 7.5 to 8.1 $\text{MPa}\sqrt{\text{m}}$, nearly twice the room-temperature toughness. The IM1 alloy, however, had a toughness exceeding 10 $\text{MPa}\sqrt{\text{m}}$ at 800 °C and 1200 °C, whereas at 1300 °C, a steeply rising R curve was seen with the toughness increasing from an initial value of $K_0 \sim 9.7 \text{ MPa}\sqrt{\text{m}}$ at crack initiation to a steady-state value of $K_{ss} \sim 11.7 \text{ MPa}\sqrt{\text{m}}$ after $\sim 400 \mu\text{m}$ of crack extension.
- (6) In general, the coarser microstructures with the largest volume fraction of the α -Mo phase displayed the higher toughness. In addition, the contiguity of the α -Mo phase was also found to be closely related to the fracture toughness, because crack trapping is the dominant toughening mechanism in these alloys, as subsequently discussed in section IV. Indeed, the order of the degree of contiguity is in a good agreement with that of the fracture toughness values experimentally measured for the alloys (Table II).

Specific crack-initiation and steady-state toughness values for all alloys are listed in Table IV.

Figure 4 shows scanning electron micrographs of the corresponding fracture surfaces for the IM1, PM1, and PM2 alloys. It is apparent that fracture at 25 °C is predominantly brittle and transgranular in nature. The fracture surface of the lowest toughness PM1 alloy is particularly flat, shiny, and “brittlelike” in appearance (Figure 4(b)). As noted in the prior study on IM1,^[7] fracture at ambient temperatures is associated with crack trapping by the larger ($>30 \mu\text{m}$) α -Mo particles. Crack paths (Figure 5) tend to be predominantly confined to the intermetallic matrix and the Mo/matrix interfaces, with the crack tending to circumvent or crack many of the smaller ($\leq 10 \mu\text{m}$) spherical particles and eventually fracturing through the larger ($>30 \mu\text{m}$) elongated ones. There is little evidence of plastic stretching in the Mo phase. Indeed, the particlelike features on the fracture surfaces (Figure 4) are associated with the smaller α -Mo regions; they show few signs of interaction with the brittle fracture of the intermetallic matrix and show little evidence of plastic deformation prior to failure (Figure 4(a)). There is evidence of some of the larger α -Mo particles remaining unbroken in the crack wake, but the fact that so little deformation of the Mo phase occurs when it breaks indicates the effect of the constraint by the surrounding intermetallic matrix in limiting the ductility of the Mo phase and hence minimizing the degree of ductile-phase bridging. A typical crack/particle interaction in the coarser-grained IM1 alloy at 25 °C involves the main crack first being trapped by a

Table IV. Fatigue Toughness and Fatigue Threshold ($R = 0.1$) Values

Alloy	Temperature (°C)	Initiation Toughness, K_0 (MPa \sqrt{m})	Steady-State Toughness, K_{ss} (MPa \sqrt{m})	Fatigue Threshold ΔK_{th} (MPa \sqrt{m})	Fatigue Threshold $K_{max,th}$ (MPa \sqrt{m})
IM1*	25	7.2	7.8	4.9	5.4
	1300	9.7	11.7	7.5	8.3
PM1	25	4.1	(4.1)	**	4.1
	1300	8.1	(8.1)	—	8.1
PM2	25	5.7	(5.7)	4.7	5.2
	1300	7.5	7.7	—	—
IM2	25	6.3	6.7	3.7	4.1
MoSi ₂ †	25	~4.0	(~4.0)	**	~4.0
MoSi ₂ /Nb _p †	25	5.2	(5.2)	~2.0	~2.2

*Prior results from Ref. 7; this reference also contains additional data for IM1 at 800 °C and 1200 °C.

**No fatigue-crack growth is detected; samples fail catastrophically when $K_{max} \sim K_0$.

†Prior results from Ref. 4.

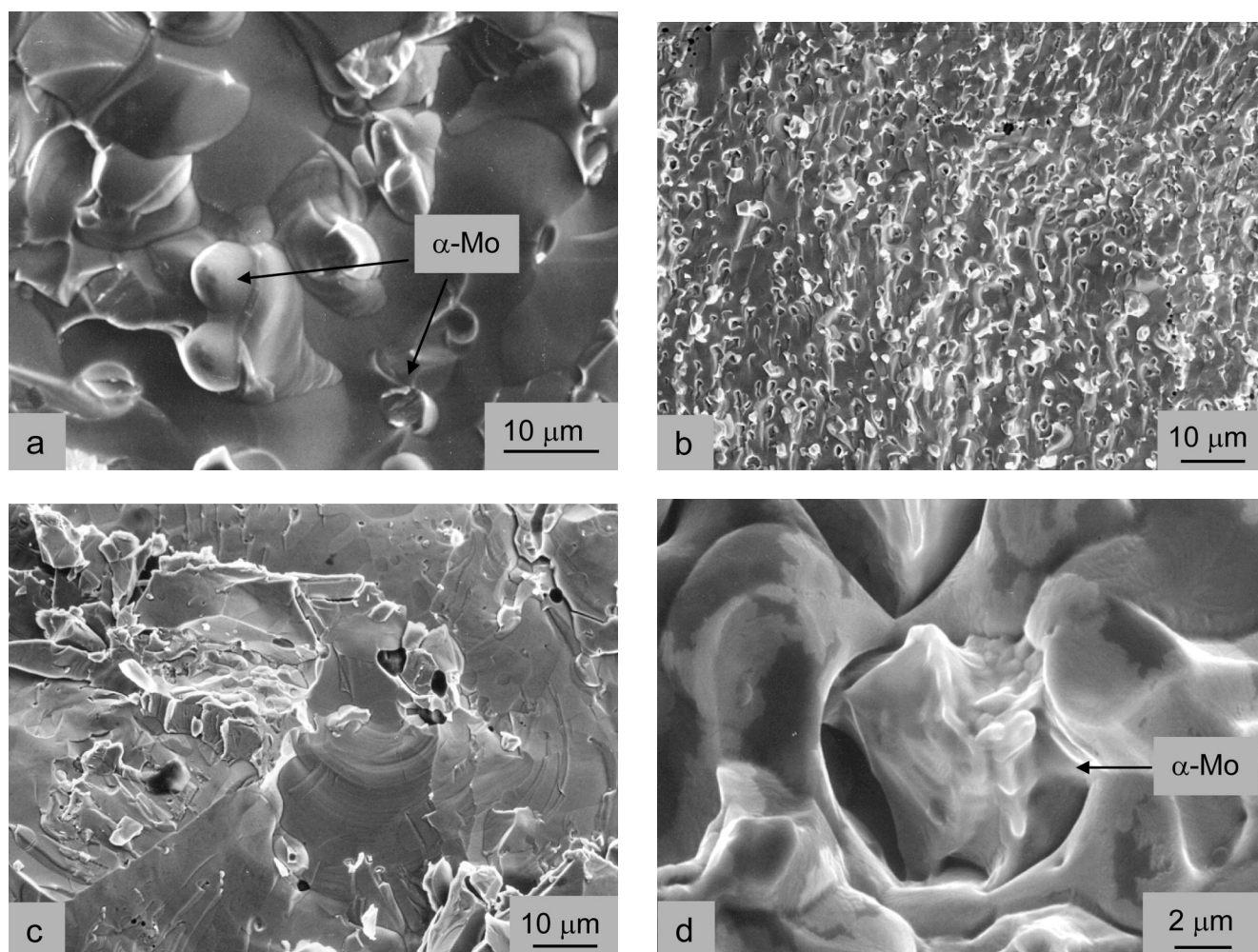


Fig. 4—Scanning electron micrographs of fracture surfaces in Mo-Si-B alloys: (a) IM1 at 25 °C, (b) PM1 at 25 °C, (c) PM2 at 25 °C, and (d) IM1 at 1300 °C, under monotonic loading showing brittle transgranular fracture. Note the failure of the Mo particles in the IM1 alloy; little evidence of plastic deformation can be seen at ambient temperature (a), whereas significant plastic stretching and debonding is apparent at 1300 °C (d). Fractographic features are nominally similar under cyclic loading.

large ($\sim 30 \mu\text{m}$) α -Mo region (Figure 5). With increasing applied stress, several microcracks form around the main crack and open as the main crack moves on leaving the Mo phase unbroken in the crack wake; the main crack is then

arrested at the next large α -Mo region and the process repeats itself. At low temperatures, however, the resultant ductile-phase bridging in the crack wake is limited by the low ductility of the Mo phase.

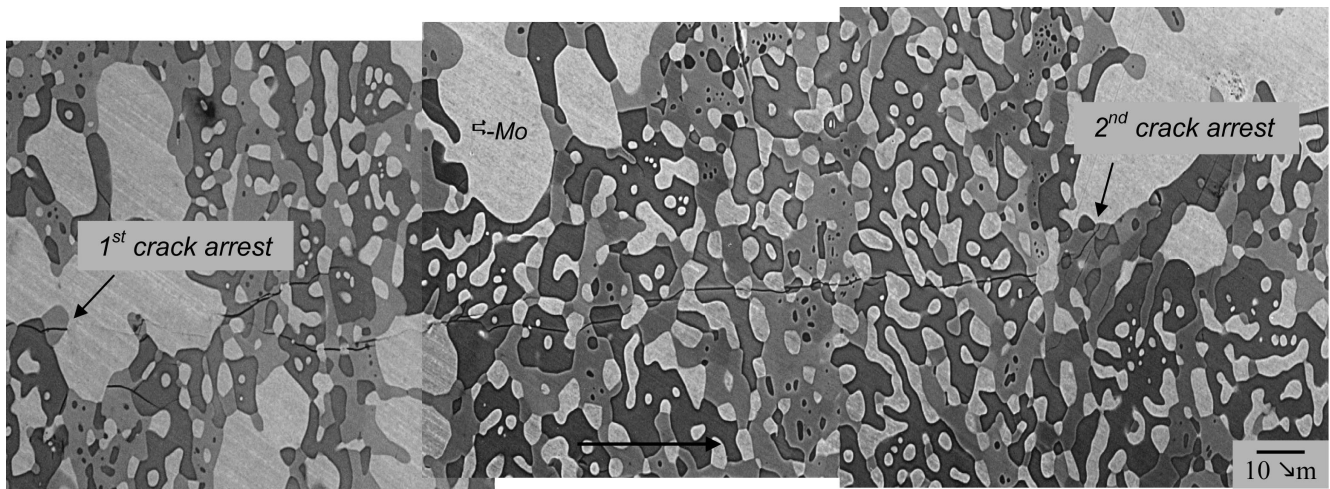


Fig. 5—The interaction of crack path with microstructure in IM1 alloy at 25 °C: at a ΔK of $\sim 7 \text{ MPa}\sqrt{\text{m}}$, crack advance was first arrested at the large α -Mo particle on the left-hand side of the micrograph. Following some degree of microcrack formation around the particle, the main crack propagated through the particle, and progressed some $\sim 200 \mu\text{m}$ before being retrapped at another large ($>30 \mu\text{m}$) α -Mo region. The horizontal arrow represents the direction of crack growth.

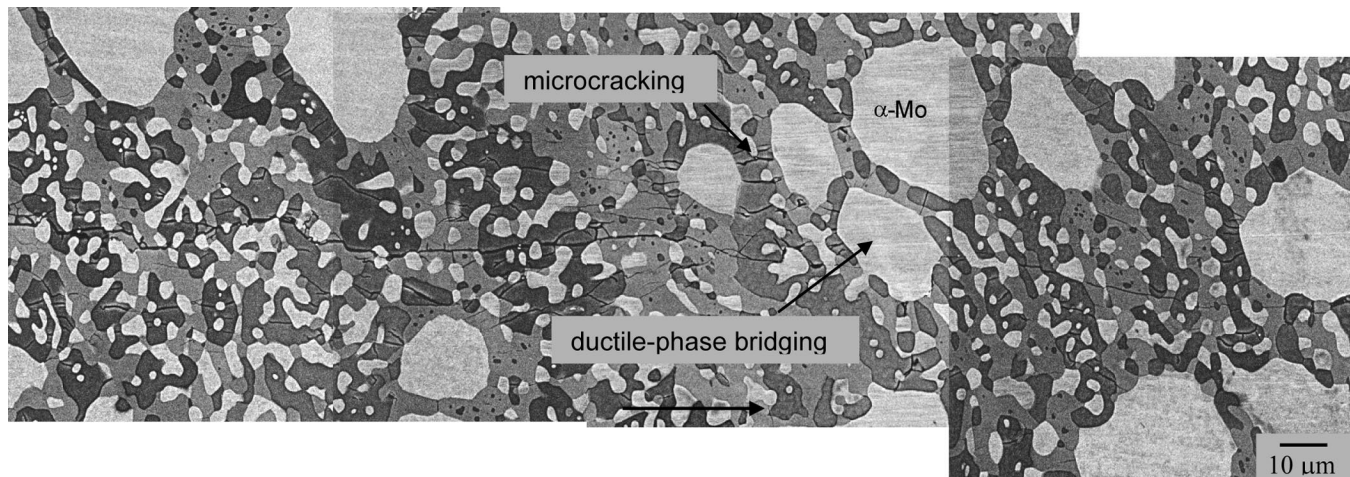


Fig. 6—The interaction of crack path with microstructure in IM1 alloy at 1300 °C, showing ductile-phase bridging by the large α -Mo particles and extensive microcracking in the Mo_5SiB_2 phase parallel to the main crack path. The horizontal arrow represents the direction of crack growth.

At elevated temperatures (800 °C to 1300 °C), however, above the ductile-brittle transition temperature of molybdenum,* a significant amount of stretching and debonding of

*Depending upon purity and processing history, the ductile-brittle transition temperature of molybdenum is between $\sim 50 \text{ °C}$ and 500 °C .^[28,29]

the α -Mo phase from the $\text{Mo}_3\text{Si}/\text{Mo}_5\text{SiB}_2$ matrix can be seen prior to failure of the Mo particles (Figure 4(d)). In the coarser-grained I/M alloys, this results in significantly increased toughening, primarily from crack bridging by unbroken α -Mo particles in the crack wake (Figure 6). In addition, there is evidence of extensive microcracking, parallel to the main crack tip. Such microcracking is predominantly contained in the Mo_5SiB_2 phase and invariably arrests at the α -Mo, presumably because of the higher ductility of molybdenum at these temperatures.

D. Fatigue-Crack Propagation Behavior

The variation in the cyclic fatigue-crack propagation rates, da/dN , with the maximum and alternating stress intensities,

K_{max} and ΔK , respectively, at $R = 0.1$ for Mo-Si-B alloys IM1, IM2, and PM2 at 25 °C and alloy IM1 at 800 °C to 1300 °C is shown in Figure 7; fatigue threshold values are listed in Table III. Corresponding stable fatigue-crack growth in alloy PM1 could not be obtained as samples failed catastrophically at $\Delta K \sim 4 \text{ MPa}\sqrt{\text{m}}$ after less than $30 \mu\text{m}$ of apparent crack extension. Results for the Mo-Si-B alloys, which span growth rates from $<10^{-10}$ to 10^{-6} m/cycle, are compared in Figure 7 with previous data on the monolithic MoSi_2 .^[4]

At ambient temperatures, the optimal resistance to fatigue-crack growth, in the form of the highest ΔK_{th} or $K_{\text{max,th}}$ fatigue thresholds, was found in the coarser-grained IM1 alloy; the somewhat finer-scale IM2 alloy had an approximately 30 pct lower threshold. Despite its lower toughness, the PM2 alloy showed a room-temperature threshold close to that of the IM1 alloy; back-face strain compliance measurements, which are routinely used to monitor crack closure,^[30] suggested that this anisotropic microstructure, with large elongated α -Mo particles, was somewhat more effective in promoting crack deflection and (roughness-induced)

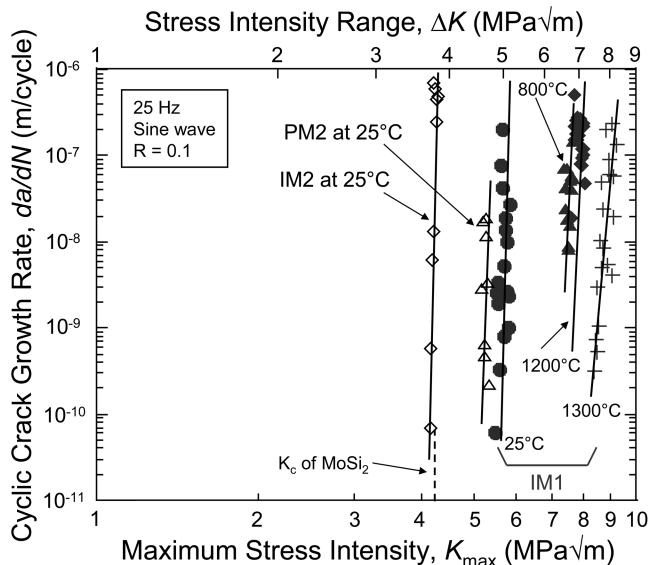


Fig. 7—Variation in cyclic fatigue-crack propagation rates, da/dN , as a function of the applied maximum, K_{max} , and alternating, ΔK , stress intensities, in the boron-modified molybdenum silicide alloys at a load ratio R of 0.1 between 25 °C and 1300 °C. Shown for comparison are previous results^[4] for monolithic $MoSi_2$.

crack closure. In general, though, higher toughness equated to improved fatigue resistance, with the $K_{max,th}$ threshold being on the order of $0.7 K_{Ic}$ in the I/M alloys and $\sim K_0 = K_{Ic}$ in the P/M alloys (which essentially displayed a minimal sensitivity to fatigue).

With an increase in temperature, resistance to fatigue-crack propagation was enhanced, at least in the IM1, IM2, and PM2 alloys that were evaluated. Fatigue thresholds, ΔK_{th} , in IM1 were increased from $\sim 5 \text{ MPa}\sqrt{\text{m}}$ at 25 °C to over $7 \text{ MPa}\sqrt{\text{m}}$ at 1200 °C to 1300 °C. Indeed, it is apparent that both toughness and fatigue resistance are increased with increasing temperature in these alloys (Figure 8).

Similar to most brittle ceramics and intermetallics, however, cyclic crack-growth rates in these alloys were strongly dependent upon ΔK (or more precisely with the prime dependency on K_{max}) and displayed steep, linear, growth-rate curves.^[31,32] In terms of a Paris power-law expression, $da/dN \propto \Delta K^m$, the exponent, m , for these alloys was extremely high and comparable to those measured in untoughened ceramics, where m can be as high as 50 or more.^[33] Due to improved ductility, the value of this exponent decreased with temperature: at 25 °C, $m \sim 60$; between 800 °C and 1200 °C, it is ~ 55 ; and at 1300 °C, it drops to ~ 44 .

Crack-particle interactions in the Mo-Si-B alloys under cyclic loading were observed to be quite similar to those under monotonic loading. In general, fatigue cracks at ambient temperatures tended to propagate through, or around, the smaller ($< 10 \mu\text{m}$) α -Mo particles and arrest at the larger ones. However, at increasing temperatures, only limited ductile-phase bridging by the α -Mo phase was detected, although extensive microcracking in the Mo_5SiB_2 regions was again seen parallel to the main crack path.

IV. DISCUSSION

On the basis of several recent studies,^[1-3,7,11-18] boron-containing molybdenum silicide alloys appear to offer good

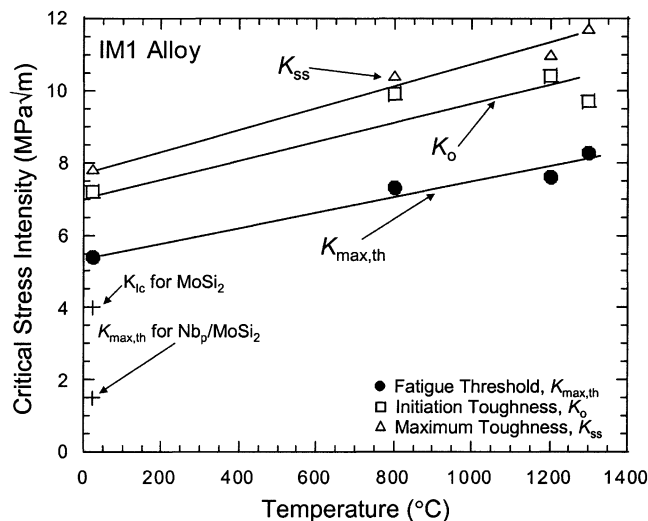


Fig. 8—Results showing the increase in the $K_{max,th}$ fatigue threshold in Mo-B-Si alloy IM1 with increase in temperature, in comparison to the corresponding increase in fracture toughness, in terms of the crack initiation, K_0 , and steady-state, K_{ss} , toughnesses on the R curve. Previous data^[4] for $MoSi_2$ are shown for comparison.

potential for future very-high-temperature structural alloys. Of these, alloys containing Mo_3Si and T2, with α -Mo to promote ductile-phase toughening and boron to promote resistance to intermediate temperature oxidation (pesteing), appear to be stable and superior to $MoSi_2$ and Mo_5Si_3 , both in terms of pesteing resistance and low-temperature toughness properties. In the present work, alloys based on the nominal composition (in at. pct) Mo-(12-17)Si-8.5B, comprising ~ 21 -38 vol. pct α -Mo within an intermetallic matrix of Mo_3Si and Mo_5SiB_2 , have been shown (1) to be more resistant to pesteing than Mo-Si alloys, primarily due to the formation of a low-viscosity protective scale of borosilicate glass (refer also to References 12 through 18); and (2) to provide much improved fracture toughness and crack-growth resistance compared to $MoSi_2$. Moreover, what is perhaps most impressive about these alloys is that their toughness and crack-growth resistance appear to improve with an increase in temperature up to 1300 °C.

It is important to note, however, that the superior fracture toughness (and fatigue) properties are only realized with specific microstructures. Although the coarse-grained I/M alloy, IM1, develops an ambient-temperature toughness that is almost double that of unreinforced $MoSi_2$, the much finer-grained P/M microstructure, PM1, which contains ~ 50 pct lower α -Mo volume fraction, has a toughness of only $4 \text{ MPa}\sqrt{\text{m}}$, which is no better than $MoSi_2$. Similarly, at a fixed volume fraction of α -Mo, the PM2 alloy has roughly twice the average α -Mo particle size with twice the contiguity compared to the PM1 alloy, consistent with its ~ 40 pct higher toughness.

In Section IV-A, we examine the various toughening mechanisms involved, the influence of microstructure in promoting these mechanisms, and their comparative effect on resistance to fatigue-crack propagation, at both ambient and elevated temperatures.

A. Toughening Mechanisms

The toughening of a brittle matrix with a ductile phase can be achieved through *extrinsic* toughening mechanisms

such as ductile-phase bridging and microcracking.^[32] These mechanisms can impede crack growth through a process of crack-tip shielding in the crack wake, which acts to “shield” the crack tip from the full applied driving force; as such, they promote *crack-growth toughness* in the form of a rising R curve. Crack trapping, where the main crack is impeded by the presence of a particle or phase and must renucleate across, or bow around, this entity, is an *intrinsic* toughening mechanism, which, conversely, tends to enhance the *crack-initiation toughness*. In addition to their effect on the R curve, these classes of toughening mechanisms have other important distinctions, notably that intrinsic mechanisms are equally effective under fatigue loading, whereas extrinsic mechanisms tend to degrade under cyclic loads. Indeed, there is ample evidence that ductile-phase bridging in an intermetallic matrix is relatively ineffective under cyclic loading because the ductile bridges tend to fail prematurely by fatigue.^[4,32,34–36]

In the current work, fractographic and crack-path observations imply that there are three primary toughening mechanisms in Mo-Si-B alloys:

- (1) crack trapping, principally by the α -Mo phase, at ambient temperatures;
- (2) additional ductile-phase bridging, again by the α -Mo phase, at elevated temperatures; and
- (3) microcracking, within the Mo₅SiB₂ phase, exclusively at elevated temperatures.

Of the four alloys tested at 25 °C, the coarsest-scale I/M alloy, IM1, exhibits the highest initiation toughness ($K_0 \sim 7.2 \text{ MPa}\sqrt{\text{m}}$), followed by IM2 ($\sim 6.3 \text{ MPa}\sqrt{\text{m}}$); the finer-scale P/M alloys, with their lower α -Mo content, show the lowest toughnesses, *i.e.*, $\sim 5.7 \text{ MPa}\sqrt{\text{m}}$ for alloy PM2 and $\sim 4.1 \text{ MPa}\sqrt{\text{m}}$ for alloy PM1. This same ranking applies at elevated temperatures and is true for both the initiation and steady-state toughness values. This implies that the alloys with a higher fraction of large α -Mo particles, and hence the smaller “effective” interparticle spacing, exhibit higher fracture toughness than those with low volume fractions and finer α -Mo particles. Indeed, microstructural observations clearly show how cracks are locally arrested at the larger Mo regions, typically, greater than $\sim 30 \mu\text{m}$, as opposed to propagating through, or around, the smaller ones (Figure 5). Moreover, compared to the IM2 alloy, which displays the second coarsest distribution of α -Mo, the IM1 microstructure has the larger degree of clustering of the α -Mo phase, which results in semicontinuous Mo regions (Figure 1(a)). Because this increases the probability of the crack intercepting the ductile phase, such coarse, semicontinuous Mo regions can be considered to enhance the effectiveness of both the crack trapping and ductile-phase bridging mechanisms. Indeed, compared to the PM1, which is the most brittle, and the finest scale of the four alloys, the IM1 alloy has a factor of 5 times larger average size of α -Mo particles (Table II). Moreover, as noted previously, the PM2 alloy has ~ 40 pct higher toughness than the PM1 alloy, consistent with its larger and more contiguous α -Mo regions; when the α -Mo volume fraction is increased, as in the IM1 and IM2 alloys, the toughness is increased even further, by ~ 50 to 75 pct.

1. Low-temperature toughening

a. Unconstrained crack trapping

Crack trapping is a common toughening mechanism for brittle materials reinforced with ductile phases.^[37,38] As an intrinsic toughening process, it does not result in a rising R curve due to the absence of a process zone, but instead acts to enhance the crack-initiation toughness; furthermore, it is effective in fatigue. Both characteristics are shown by the alloys in the present study (Figures 3 and 7).

Such trapping appears to be the dominant toughening mechanism in Mo-Si-B alloys at 25 °C, although it is still active at elevated temperatures. At ambient temperatures, the toughening effect of the crack bridging by the intact ductile particles appears to be comparatively minor, presumably due to the limited ductility of Mo at 25 °C,^[29,30] this results in the Mo-Si-B alloys displaying relatively shallow R curves at lower temperatures, as shown in Figure 3.

As noted previously, the trapping process involves crack arrest primarily at the larger α -Mo particles, subsequent microcrack formation ahead of the crack tip, and renucleation of the crack across the particle, either by bowing out between the pinning regions or propagating through the particle (Figure 5). The increase in crack-initiation toughness with increasing volume fraction, size, and changing morphology of the α -Mo phase is consistent with this mechanism, as shown by the ambient-temperature K_0 data for the four alloys in Figure 3. Such trapping and bowing of the crack front has been modeled by the Bower and Ortiz model^[37] in terms of a spherical array of ductile crack-trapping particles embedded in a brittle matrix, where the toughness of the “composite,” K_c , can be expressed in terms of the relative toughness of the brittle matrix, K_c^b , and the ductile particles, K_c^d , as

$$K_{Ic} \approx K_c^b \left\{ 1 + \frac{2r}{l} \left[\left(\frac{K_c^d}{K_c^b} \right)^2 - 1 \right] \right\}^{1/2} \quad [1]$$

where r is the characteristic dimension of the trapping particles and l is their average spacing. Quantitatively, using a fracture toughness for Mo at 25 °C of $K_c^d \sim 15 \text{ MPa}\sqrt{\text{m}}$ ^[39,40] and for the Mo₃Si/Mo₅SiB₂ matrix of $K_c^b \sim 3 \text{ MPa}\sqrt{\text{m}}$,^[6] and average values (based on crack profile measurements) of r/l ranging from ~ 0.2 (for alloy IM1) to 0 (for alloy PM1), estimates of the ambient-temperature crack-initiation toughness were calculated from Eq. [1] and are listed in Table V. Despite the uncertainties involved*,

*The precise toughness of the α -Mo phase is difficult to assess because small amounts of interstitial impurities, such as oxygen, can severely embrittle molybdenum at ambient temperatures.^[40]

the predicted toughness values due solely to crack trapping are reasonably close to the experimentally measured values, and exactly reflect the ranking of the alloys.

Although Eq. [1] does not take into account the shape of α -Mo particles, it was apparent from crack profiles showing the crack/ α -Mo particle interactions that crack trapping was more effective at irregular, rather than spherically, shaped particles. This observation is consistent with previous studies on MoSi₂, where composite alloys reinforced with Nb wires exhibited far higher toughnesses than those containing Nb particulate.^[35]

Table V. Crack-Initiation Toughness Prediction Based on Crack Trapping

Alloy	r , Characteristic Dimension (μm)	l , Effective Spacing* (μm)	$2r/l$	Calculated K_{Ic} Toughness ($\text{MPa}\sqrt{\text{m}}$)	Experimental K_{Ic} Toughness ($\text{MPa}\sqrt{\text{m}}$)
IM1	10.43	50	0.42	9.8	7.2
IM2	6.99	50	0.14	6.5	6.3
PM1	2.14	∞	0	3.5	4.1**
PM2	4.41	50	0.09	5.6	5.7

*Effective spacing, l , is defined as an average distance between the large (trapping) α -Mo particles (≥ 20 to $30 \mu\text{m}$).

**This represents an indentation toughness, which is used instead of the more conventional techniques due to the extreme brittleness of alloy PM1.

b. Constrained crack trapping

The Bower and Ortiz model^[37] also does not consider the critical role of the hard phase in creating high plastic constraint (in the form of an increased hydrostatic stress state) in the more ductile phase, as recently pointed out by Chan and Davidson.^[41] This constraint acts to limit the ductility of the ductile phase and hence to limit the degree of ductile-phase toughening. The latter authors, by considering the constraint issue, derived an expression for the “composite” fracture toughness, K_{Ic} , in terms of the respective toughnesses of the ductile and brittle phases, K_c^d and K_c^b , and the volume fraction of the brittle phase, f_b , at which hard particles begin to make contact, f_{crit} .^[41]

$$K_{Ic} = K_c^b \left(1 + (1 - f)^{1/2} \left[\left(\frac{K_c^d}{K_c^b} \right)^2 \exp \left(-\frac{8q}{3} \left(\frac{f}{1-f} \right) \right) - 1 \right] \right)^{1/2} \quad [2]$$

where q is a factor that varies with particle geometry (taken to be unity in the present case), and $f = f_b$ for $f_b < f_{crit}$ and $f = f_{crit}$ for $f_b \geq f_{crit}$. For the present series of alloys, where the brittle $\text{Mo}_3\text{Si}/\text{Mo}_5\text{SiB}_2$ phase constitutes the matrix, *i.e.*, f_b is always greater than f_{crit} , the room-temperature toughness predicted from Eq. [2] will be the same for all four alloys and will be quite sensitive to the chosen value of f_{crit} . As this latter value is difficult to estimate, this relationship has limited utility in predicting the toughness of the current alloys. However, the measured range of toughnesses, *i.e.*, from $\sim 3 \text{ MPa}\sqrt{\text{m}}$ for the untoughened intermetallics matrix to $\sim 7 \text{ MPa}\sqrt{\text{m}}$ for the “best” toughened alloy, are consistent with reasonable f_{crit} values between 0.40 and 0.55.

c. Comparison with rule of mixtures

Again, following the approach of Chan and Davidson,^[41] it is pertinent to compare these estimates for the room-temperature toughness of these alloys with that based on the rule of mixtures, where

$$K_{Ic} = K_c^b \left[f_b + (1 - f_b) \left(\frac{K_c^d}{K_c^b} \right)^2 \right]^{1/2} \quad [3]$$

This is shown in Figure 9, where the experimental room-temperature toughness values for the four Mo-Si-B alloys are compared to predictions based on Eq. [3] and the crack trapping models for unconstrained^[37,41] and constrained (Eq. [2]^[41]) plasticity in the ductile phase.* The trapping model

*Note that the prediction for crack trapping without plastic constraint used in Figure 9 is based on the Chan and Davidson^[41] derivation of the Bower and Ortiz^[37] analysis and as such does not directly include terms

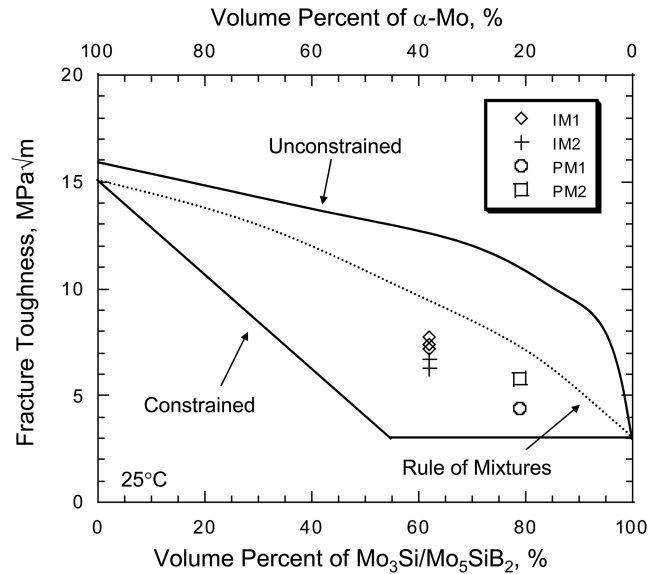


Fig. 9—Comparison of the experimental room-temperature fracture toughness data for the I/M and P/M Mo-Si-B alloys to theoretical calculations based on the rule of mixtures^[41] and models for crack trapping, which consider unconstrained^[37,41] and constrained^[41] plasticity in the ductile phase.

based on the size and spacing of the trapping phase. In addition, for the predictions based on the trapping model with plastic constraint,^[41] a value of $f_{crit} = 0.55$ has been assumed.

calculations in the absence of plastic constraint can be seen to severely overpredict toughness, with the implication that the decrease in toughness with increasing volume fraction of the intermetallic $\text{Mo}_3\text{Si}/\text{Mo}_5\text{SiB}_2$ phase may be related to an increase in matrix constraint on the α -Mo particles. Moreover, as the experimentally measured values are lower than that predicted by the rule of mixtures, one can interpret (in Chan and Davidson’s terminology^[41]) the room-temperature toughening behavior in these alloys as a “brittle-phase embrittlement,” rather than a “ductile-phase toughening” *per se*.

2. High-temperature toughening

a. Ductile-phase bridging

Crack trapping by the larger α -Mo regions can lead to some degree of crack bridging by intact Mo regions in the crack wake; however, because of the apparent low ductility of Mo at ambient temperatures, this mechanism does not appear to be particularly effective at $25 \text{ }^\circ\text{C}$, as evidenced by

the relatively flat R curves. Similar effects have been reported where other refractory metals, such as Mo, V, Cr, or W, have been selected as bridging phases, simply because of their minimal ductility at these temperatures.^[42] However, with the increased ductility of the metal phase at elevated temperatures (as evidenced by the ductile nature of their fracture in Figure 4), this extrinsic toughening mechanism appears to be far more effective (Figure 6) and results in more pronounced R -curve behavior, as is particularly apparent for the IM1 alloy at 1300 °C (Figure 3).

As described previously,^[7] the magnitude of such toughening can be estimated (for small-scale bridging) from the increase in energy associated with particle deformation and failure in the wake of the crack,^[43] viz.

$$K_{Ic} \approx [(K_c^b)^2 + f_d E' \sigma_0 r \chi]^{1/2} \quad [4]$$

In Eq. [3], K_c^b is the crack-initiation toughness of the brittle matrix, E' is the plane-strain elastic modulus of the composite; and χ is the dimensionless work of rupture of the reinforcement, or the area under the normalized stress [$\sigma(u)$]-

displacement [u] function, $\int_0^{u^*} (\sigma(u) du / \sigma_0 r)$, where σ_0 and f_d are, respectively, the yield strength and volume fraction of ductile (bridging) phase and u^* is the critical crack-opening displacement for its fracture.^[43,44]

Taking values for the Mo-Si-B alloys at 1300 °C for E' of ~ 179 GPa with σ_0 for α -Mo of ~ 103 MPa^[5,6,35] and a matrix toughness for Mo₃Si/Mo₅SiB₂ of $K_c^b \sim 3.5$ MPa \sqrt{m} ,^[6] estimates of the degree of steady-state toughening at elevated temperatures can be made, assuming a value of χ of 3 based on the tensile properties of Mo at 1300 °C.^[45,46] From metallographic sectioning, a reasonable average dimension of the bridging α -Mo particles at 1300 °C for the IM1 alloy is $r \sim 5$ μm ,^[7] which gives a predicted value of the toughness due solely to bridging in this alloy of $K_{Ic} \sim 10.8$ MPa \sqrt{m} , *i.e.*, comparable to the experimentally measured K_{Ic} value of ~ 11.7 MPa \sqrt{m} at 1300 °C. Smaller values of r , *i.e.*, between ~ 1 and 4 μm , yield predicted toughnesses between 5 and 8 MPa \sqrt{m} , respectively, for the other alloys studied. Although these estimates cannot be directly compared with the experimental measurements, in particular, because the P/M alloys show little evidence of R -curve toughening, they are consistent with the lower toughness properties displayed by these alloys, which all have a lower volume fraction or smaller particle size of the α -Mo phase.

b. Microcracking toughening

As noted previously,^[7] an additional, yet smaller, source of toughening in Mo-Si-B alloys can arise at elevated temperatures from microcracking, as shown in Figure 6 by the zone of microcracks, arrested between α -Mo regions, in layers parallel to the main crack path. The microcracks form in the Mo₅SiB₂ phase, presumably because of its higher thermal expansion and tetragonal crystal structure, compared to the Mo and Mo₃Si phases (which are both cubic). As the coefficient of thermal expansion of Mo at 1300 °C is ~ 25 pct lower than that of Mo₅SiB₂,^[47,48] the microcracking would be expected to form in the latter phase and to be parallel to the main crack, *i.e.*, perpendicular to the applied tensile stresses.

Models for microcrack toughening^[49–56] are based on (1) the volume displaced by the microcracks and (2) the resulting reduction in the elastic modulus within the process zone. The increase in toughness at steady state can be estimated in terms of the closure stress intensity for such dilatational toughening^[54,57] and the modulus reduction^[50,58] as

$$\Delta K_c^{\text{mic}} \approx 0.22 \varepsilon E' f_m h^{1/2} + \beta f_m K_c^b \quad [5]$$

where E' is the plane strain elastic modulus, f_m is the volume fraction of microcracks, ε is the dilatational strain, and h is the height of microcrack zone. The second term represents the compliance toughening, where β is a parameter (~ 1.2)^[58] that depends on Poisson's ratio and the matrix toughness ($K_c^b \sim 3.5$ MPa \sqrt{m})^[3]. Direct measurements of crack profiles gave approximate values of $f_m \sim 0.15$ in the microcracking zone, and the height of this zone as $h \sim 20$ μm . Taking the residual volumetric strain as $\varepsilon \sim 0.06$, estimates of the maximum microcrack toughening for the IM1 alloy at 1300 °C suggest a small increase in toughness of ~ 2 MPa \sqrt{m} due to dilatation toughening and a further ~ 1 MPa \sqrt{m} from the compliance change.

B. Fatigue-Crack Propagation

Characteristic of many brittle intermetallic and ceramic materials,^[32] fatigue-crack propagation in the Mo-Si-B alloys is extremely sensitive to the applied stress intensities (Figure 7), *i.e.*, to the stresses and crack size, which results in very high exponent m values in the Paris law relationship. Despite these high values, resistance to fatigue-crack growth in terms of the specific fatigue thresholds (Table IV) is, in general, far larger in the present boron-doped molybdenum silicides than in monolithic MoSi₂ (which simply fails catastrophically at $K_{Ic} \sim 3$ to 4 MPa \sqrt{m}) or in MoSi₂ reinforced with Nb spheres (Nb_p/MoSi₂).^[14] However, similar to the fracture toughness behavior, these superior fatigue properties are not realized in all Mo-Si-B microstructures.

In general, the coarser microstructures with the higher α -Mo content that develop the higher toughnesses display the better fatigue-crack growth resistance; specifically, in the I/M Mo-Si-B alloys, $K_{\text{max,th}}$ thresholds are nominally 70 pct of the steady-state toughness values. Indeed at 25 °C, the $K_{\text{max,th}}$ threshold for the toughest alloy IM1 is over 5 MPa \sqrt{m} , compared to ~ 2 MPa \sqrt{m} in Nb_p/MoSi₂.^[4] Moreover, akin to the toughness, the threshold values are even higher at elevated temperatures, rising in the IM1 alloy to over 8 MPa \sqrt{m} at 1300 °C. This results from the coupled nature of the fracture toughness and fatigue-crack growth properties in brittle solids such as molybdenum silicides. As noted previously, the toughness is increased at elevated temperatures primarily due to the improved high-temperature ductility of α -Mo phase, which results in the onset of additional (extrinsic) toughening mechanisms, namely, microcracking and more significantly ductile-phase bridging. However, due to premature fatigue of the bridging α -Mo particles in the crack wake, the latter mechanism appears to degrade under cyclic loading leading to subcritical crack growth at lower applied K levels, similar to behavior reported for ductile-phase-toughened MoSi₂, γ -TiAl, and Nb₃Al intermetallics.^[34,35,36] It is likely that, except for crack growth in the Mo regions at temperatures above ambient, fatigue-

crack growth in these alloys occurs, as in most brittle solids,^[32] primarily by the cyclic-loading induced suppression of extrinsic toughening in the crack wake, with the actual crack advance mechanism being essentially identical to that under monotonic loads. Such a mechanism is totally consistent with the lack of any significant change in the fracture morphology under monotonic and cyclic loading, and more importantly with the extremely high sensitivity of growth rates to the applied stress intensities, *i.e.*, to very high m exponents.

In light of this large dependency on applied stress intensities, the use of these intermetallics for safety-critical structural applications subject to cyclic loading will increasingly require reliable in-service fatigue lifetime prediction. The extremely high m values are actually indicative of a minimal susceptibility to fatigue failure; however, they do imply that the cycles or time to failure will be extremely sensitive to crack size and the applied stress. For this reason, the use of traditional damage-tolerant approaches for lifetime prediction, which rely on the integration of $(da/dN)/K$ curves to estimate the time for a presumed initial crack to grow to failure, may prove difficult to use in practice.^[33] However, because subcritical crack growth under cyclic loading can definitely occur in these alloys, a more reasonable basis for design with these materials would appear to be through the use of the $K_{\max,th}$ (or ΔK_{th}) fatigue threshold, which in these alloys is typically ~ 70 to 100 pct of the highest toughness on the R curve; indeed, in the limit, $K_{\max,th} \rightarrow K_0$. In this regard, it is pertinent to note in conclusion that the threshold values measured in this work for the tougher I/M alloys are certainly comparable at ambient temperatures with many metallic alloys, but are far superior to any metallic material at temperatures above 1000 °C.

V. CONCLUSIONS

Based on a study, at ambient to elevated temperatures (25 °C to 1300 °C), of the fracture toughness, fatigue-crack propagation and peeling properties of a range of I/M and P/M boron-containing molybdenum silicide (Mo/12 to 17 at. pct Si/8.5 at. pct B) alloys, comprising ~ 21 to 38 vol. pct α -Mo phase in an intermetallic matrix of Mo_3Si and Mo_5SiB_2 (T_2), the following conclusions can be made.

1. Boron-modified molybdenum silicide alloys display an improved pest resistance at 400 °C to 900 °C as compared to unmodified molybdenum silicides, such as Mo_5Si_3 , although the weight losses at ~ 800 °C are still of some concern. The improved pest resistance compared to Mo_5Si_3 , however, results from the formation of a semi-protective layer of borosilicate glass ($\text{B}_2\text{O}_3/\text{SiO}_2$), which (1) provides a degree of protection that increases with increasing temperature and (2) has sufficient fluidity (compared to SiO_2) at lower temperatures to flow into cracks and voids to protect the alloy surface.
2. In their ingot-metallurgy processed form, these Mo-Si-B alloys, which contain a higher volume fraction of relatively ductile α -Mo regions, provide a marked increase in the ambient to high-temperature fracture toughness properties compared to conventional monolithic molybdenum silicides, such as MoSi_2 or Mo_5Si_3 . Fatigue-crack propagation resistance between 25 °C to 1300 °C is similarly improved. Indeed, both the fracture toughness and fatigue-crack propagation thresholds are actually increased with increasing temperature between 25 °C and 1300 °C.
3. Corresponding powder-metallurgy processed Mo-Si-B alloys, which have considerably finer-scale microstructures with ~ 50 pct lower α -Mo volume fraction, show far smaller improvements in their toughness and fatigue-crack propagation properties. Indeed, both alloys tested had, at best, only marginally better toughness properties than monolithic MoSi_2 (one was too brittle to fatigue).
4. Compared to the finer-scale P/M alloys, much improved toughness (and fatigue) properties were found with the coarser microstructures containing the high α -Mo volume fractions with large ($>30 \mu\text{m}$), more contiguous regions of this phase. Such observations were consistent with the three primary toughening mechanisms identified for these alloys, namely crack trapping, ductile-phase bridging, and microcracking.
5. At ambient temperatures, the principal toughening mechanism appeared to be crack trapping by the larger ($>30 \mu\text{m}$) α -Mo particles. As such trapping requires renucleation of the main crack across the particle, this is an intrinsic toughening mechanism, which acts to increase the crack-initiation toughness, consistent with experimental observations; consequently, only minimally rising R curves were seen at 25 °C. Microstructurally, the effect of this toughening mechanism was enhanced by increasing the volume fraction and size of the Mo particles. However, plastic constraint by the intermetallic matrix on the deformation behavior of the α -Mo particles acts to significantly limit the degree of ductile-phase toughening by this mechanism.
6. At elevated temperatures, the principal toughening mechanism appeared to be ductile-phase bridging by the larger ($>30 \mu\text{m}$) α -Mo particles that remained unbroken in the crack wake. In principle, this mechanism is also active at lower temperatures, but the much lower ductility of the Mo phase severely limited its potency. As this is an extrinsic mechanism, rising R -curve behavior was observed at the higher temperatures; this became more apparent with increasing temperature owing to the increasing ductility of the Mo. Microstructurally, the effect of this toughening mechanism was also enhanced by increasing the volume fraction and size of the α -Mo regions.
7. At elevated temperatures, small (~ 1 to $2 \text{ MPa}\sqrt{\text{m}}$) yet additional toughening was provided by microcracking, which occurred primarily in the Mo_5SiB_2 phase in the form of microcrack zones of significant dimensions ($\sim 400 \mu\text{m}$), arrested between α -Mo regions, in layers parallel to the main crack path.
8. Based on metallographic observations, high-temperature fatigue-crack propagation behavior in the tougher (I/M) Mo-Si-B alloys was reasoned to occur by the progressive degradation of the ductile-phase toughening under cyclic loading due to premature fatigue failure of the ductile, bridging phase. Nevertheless, $K_{\max,th}$ thresholds were typically 70 pct of the maximum toughness values, and in the coarsest I/M alloy to be as high as $8 \text{ MPa}\sqrt{\text{m}}$ at 1300 °C. These values, which are high even by metals standards, are far superior to those previously measured in unmodified monolithic molybdenum silicides.

ACKNOWLEDGMENTS

This work was supported by the Director, Office of Science, Office of Basic Energy Sciences, Division of Materials Sciences and Engineering, United States Department of Energy, under Contract No. DE-AC03-76SF00098, with the Lawrence Berkeley National Laboratory (for HC and ROR), and by the Office of Fossil Energy, Advanced Research Materials (ARM) Program, United States Department of Energy, under Contract No. DE-AC05-00OR22725, with Oak Ridge National Laboratory managed by UT-Battelle, LLC (for JHS). This work was part of the multi-National Laboratory program on "Design and Synthesis of Ultrahigh-Temperature Intermetallics" within the DOE Center for Excellence and Processing of Advanced Materials.

APPENDIX

Contiguity of the α -Mo phase

The contiguity of a phase in a two-phase (α - β) mixture has been defined by Gurland^[59] as the fraction of the total internal surface area of the phase shared with particles of the same phase, viz.

$$C_{\alpha} = 2S_V^{\alpha\alpha}/(2S_V^{\alpha\alpha} + S_V^{\alpha\beta}) \quad [A1]$$

where C_{α} denotes the contiguity of the α phase, $S_V^{\alpha\alpha}$ is the interface area of the α particles per unit volume, and $S_V^{\alpha\beta}$ is the area of the interfaces between α and β particles per unit volume. Following the approach of Fan *et al.*,^[60] the contiguity of the α phase therefore can be determined, using simple metallographic intercept measurements on a random plane of polish, as

$$C_{\alpha} = 2N_L^{\alpha\alpha}/(2N_L^{\alpha\alpha} + N_L^{\alpha\beta}) \quad [A2]$$

where $N_L^{\alpha\alpha}$ and $N_L^{\alpha\beta}$ are the numbers of intercepts of the α/α and α/β interfaces within a random line of unit length on the examined planes of polish. Equations [A1] and [A2] are valid for any particle size, shape, and distribution.^[60]

REFERENCES

1. M. Akinc, M.K. Meyer, M.J. Kramer, A.J. Thom, J.J. Huebsch, and B. Cook: *Mater. Sci. Eng. A*, 1999, vol. 261, pp. 16-23.
2. M.M. Meyer, M.J. Kramer, and M. Akinc: *Intermetallics*, 1996, vol. 4, pp. 273-81.
3. J.H. Schneibel, D.S. Easton, H. Choe, and R.O. Ritchie: *Proc. 3rd Int. Symp. on Structural Intermetallics*, Jackson Hole, WY, 2001.
4. K.T. Venkateswara Rao, W.O. Soboyejo, and R.O. Ritchie: *Metall. Trans. A*, 1992, vol. 23A, pp. 2249-57.
5. J.H. Schneibel, C.T. Liu, L. Heatherly, and M.J. Kramer: *Scripta Mater.*, 1998, vol. 38, pp. 1169-76.
6. J.H. Schneibel, M.J. Kramer, Ö Ünal, and R.N. Wright: *Intermetallics*, 2001, vol. 9, pp. 25-31.
7. H. Choe, D. Chen, J.H. Schneibel, and R.O. Ritchie: *Intermetallics*, 2001, vol. 9, pp. 319-29.
8. J.B. Berkowitz-Mattuck, M. Rossetti, and D.W. Lee: *Metall. Trans.*, 1970, vol. 1, pp. 479-83.
9. P.J. Meschter: *Metall. Trans. A*, 1992, vol. 23A, pp. 1763-72.
10. K. Natesan and S.C. Deevi: *Intermetallics*, 2000, vol. 8 (9-11), pp. 1147-58.
11. D.M. Berczik: U.S. Patent No. 5,595,616 and 5, 693, 156, United Technologies Corp., East Hartford, CT, 1997.
12. M.K. Meyer and M. Akinc: *J. Am. Ceram. Soc.*, 1996, vol. 79, pp. 938-44.
13. M.M. Meyer and M. Akinc: *J. Am. Ceram. Soc.*, 1996, vol. 79, pp. 2763-66.
14. M.K. Meyer, A.J. Thom, and M. Akinc: *Intermetallics*, 1999, vol. 7, pp. 153-62.
15. T. Maruyama and K. Yanagihara: *Mater. Sci. Eng. A*, 1997, vols. 239-240, pp. 828-41.
16. T.A. Parthasarathy, M.G. Mendiratta, and D. Dimiduk: *Acta Mater.*, 2002, vol. 50, pp. 1857-68.
17. X. Fan and T. Ishigaki: *J. Am. Ceram. Soc.*, 1999, vol. 82, p. 1965.
18. J.S. Park, R. Sakidja, and J.H. Perepezko: *Scripta Mater.*, 2002, vol. 46, pp. 765-70.
19. N.S. Stoloff: *Mater. Sci. Eng. A*, 1999, vol. 261, pp. 169-80.
20. *Annual Book of ASTM Standards*, ASTM, Philadelphia, PA, 1998, vol. 3.01.
21. R.H. Dauskardt and R.O. Ritchie: *Closed Loop*, 1989, vol. 17, pp. 7-17.
22. C.J. Gilbert, J.M. McNaney, R.H. Dauskardt, and R.O. Ritchie: *ASTM J. Test. Eval.*, 1994, vol. 22, pp. 117-20.
23. D. Chen, C.J. Gilbert, and R.O. Ritchie: *ASTM J. Test. Eval.*, 2000, vol. 28, pp. 236-41.
24. D. Chen, C.J. Gilbert, X.F. Zhang, and R.O. Ritchie: *Acta Mater.*, 2000, vol. 48, pp. 659-74.
25. M.G. Mendiratta, T.A. Parthasarathy, and D.M. Dimiduk: *Intermetallics*, 2002, vol. 10, pp. 225-32.
26. J. Schlichting: *J. Non-Cryst. Solids*, 1984, vol. 63, pp. 173-81.
27. J.H. Schneibel: *Proc. 16th Annual Conf. on Fossil Energy Materials*, Session IV, National Energy Technology Laboratory (NETL) Publications, Washington, DC, 2002.
28. T.E. Tietz and J.W. Wilson: *Behavior and Properties of Refractory Metals*, Stanford University Press, Stanford, CA, 1965.
29. A.Y. Koval, A.D. Vasilev, and S.A. Firstov: *Int. J. Refract. Met. Hard Mater.*, 1997, vol. 15, pp. 223-26.
30. R.O. Ritchie and W. Yu: in *Small Fatigue Cracks*, R.O. Ritchie and J. Lankford, eds., TMS, Warrendale, PA, 1986, pp. 167-89.
31. R.O. Ritchie: *Mater. Sci. Eng.*, 1988, vol. 103, pp. 15-28.
32. R.O. Ritchie: *Int. J. Fracture*, 1999, vol. 100, pp. 55-83.
33. R.O. Ritchie and R.H. Dauskardt: *J. Ceram. Soc. Jpn.*, 1991, vol. 99, pp. 1047-62.
34. K.T. Venkateswara Rao, G.R. Odette, and R.O. Ritchie: *Acta Metall. Mater.*, 1994, vol. 42, pp. 893-911.
35. K. Badrinarayanan, A.L. McKelvey, K.T. Venkateswara Rao, and R.O. Ritchie: *Metall. Mater. Trans. A*, 1996, vol. 27A, pp. 3781-92.
36. L. Murugesu, K.T. Venkateswara Rao, and R.O. Ritchie: *Scripta Metall. Mater.*, 1993, vol. 29, pp. 1107-12.
37. A.F. Bower and M. Ortiz: *J. Mech. Phys. Solids*, 1991, vol. 39, pp. 815-58.
38. J.K. Shang and R.O. Ritchie: *Acta Metall.*, 1989, vol. 38, pp. 2267-78.
39. F.E. Heredia, M.Y. He, G.E. Lucas, A.G. Evans, H.E. Dève, and D. Konitzer: *Acta Metall. Mater.*, 1993, vol. 41, pp. 505-11.
40. P. Ramasundaram, R. Bowman, and W. Soboyejo: *Mater. Sci. Eng. A*, 1998, vol. 248, pp. 132-46.
41. K.S. Chan and D.L. Davidson: *Metall. Mater. Trans. A*, 2001, vol. 32A, pp. 2717-27.
42. D.L. Davidson, K.S. Chan, and D.L. Anton: *Metall. Mater. Trans. A*, 1996, vol. 27, pp. 3007-18.
43. H.E. Dève, A.G. Evans, G.R. Odette, R. Mehrabian, M.L. Emiliani, and R.J. Hecht: *Acta Metall. Mater.*, 1990, vol. 38, pp. 1491-1502.
44. G.R. Odette, B.L. Chao, J.W. Sheckherd, and G.E. Lucas: *Acta Metall. Mater.*, 1992, vol. 40, pp. 2381-89.
45. K.S. Chan: *Metall. Trans. A*, 1992, vol. 23A, pp. 183-99.
46. R.W. Hall and P.F. Sikora: *NASA Memo 3-9-59E*, NASA, Washington, DC, 1959.
47. J.H. Schneibel, C.T. Liu, D.S. Easton, and C.A. Carmichael: *Mater. Sci. Eng. A*, 1999, vol. A261, pp. 78-83.
48. C.J. Rawn, J.H. Schneibel, C.M. Hoffman, and C.J. Hubbard: *Intermetallics*, 2001, vol. 9, pp. 209-16.
49. R.G. Hoagland and J.D. Embury: *J. Am. Ceram. Soc.*, 1980, vol. 63, pp. 404-10.
50. J.W. Hutchinson: *Acta Metall.*, 1987, vol. 35, pp. 1605-19.
51. N. Claussen and J. Steeb: *J. Am. Ceram. Soc.*, 1976, vol. 59, pp. 457-58.
52. N. Claussen: *J. Am. Ceram. Soc.*, 1976, vol. 59, pp. 49-51.
53. A.G. Evans and K.T. Faber: *J. Am. Ceram. Soc.*, 1984, vol. 67, pp. 255-60.
54. A.G. Evans and Y. Fu: *Acta Metall.*, 1985, vol. 33, pp. 1525-31.
55. A.G. Evans: *J. Am. Ceram. Soc.*, 1990, vol. 73, pp. 187-206.
56. A.A. Rubinstein: *Int. J. Fracture*, 1985, vol. 27, pp. 113-19.

57. G. Liu, D. Zhu, and J.K. Shang: *Metall. Mater. Trans. A*, 1995, vol. 26A, pp. 159-66.
58. L.S. Sigl: *Acta Mater.*, 1996, vol. 44, pp. 3599-3609.

59. J. Gurland: *Trans. TMS-AIME*, 1958, vol. 212, p. 452.
60. Z. Fan, A.P. Miodownik, and P. Tsakirooulos: *Mater. Sci. Technol.*, 1993, vol. 9, pp. 1094-1100.